The Effect of Pressure on NOx Entitlement and Reaction Timescales in a Premixed Axial Jet-in-Crossflow

Bernhard Stiehl
University of Central Florida
4000 Central Florida Blvd, Orlando, FL 32816
bernhard.stiehl@gmail.com

Michelle Otero
University of Central Florida
4000 Central Florida Blvd, Orlando, FL 32816
motero0508@gmail.com

Tommy Genova
University of Central Florida
4000 Central Florida Blvd, Orlando, FL 32816
tgenovajr@gmail.com

Scott Martin
Embry-Riddle Aeronautical University
600 S Clyde Morris Blvd, Daytona Beach, FL 32114
martis38@erau.edu

Kareem Ahmed
University of Central Florida
4000 Central Florida Blvd, Orlando, FL 32816
kareem.ahmed@ucf.edu

ABSTRACT

This paper investigates the pressure dependency of a lean premixed jet injected into a lean vitiated crossflow with an experimentally verified detailed chemistry CFD model and 53 species considered. Experimental data was taken in an axially staged combustor with an optically accessible test section, allowing the use of PIV and CH chemiluminescence techniques as well as point measurement of species concentration, temperature, and pressure. The experimental data cases at one, three and five atmospheres were selected to describe the flame stabilization dependency on pressure and gain the required knowledge for an extrapolation to engine condition. Simulated exit nitrogen oxide levels were validated with experimental emission data and a global emission trend for the NO reduction at elevated pressure and constant turbine inlet temperature level was defined. The nitrogen oxide benefit at elevated operating pressure was justified with the significantly smaller flame surface area: analysis of the simulated spanwise and top-view profiles showed a relatively short receded core flame with nitrogen oxide production in the center at high pressure relative to a longer and larger shear layer flame at atmospheric condition that produced NO towards the inner and outer side of the flame. Decomposition of the Damköhler number revealed the strong influence of the reaction timescales with higher reaction rates at elevated pressure, along with a moderate influence of the turbulent timescales, showing higher turbulence intensity in the lee-side recirculation zone at lower pressure.*

Keywords: Reacting Jet in Crossflow, Axial Fuel Staging, Axial Staged Combustion, High Pressure, Gas Turbine Combustor, NO_x Emission

1. INTRODUCTION AND OBJECTIVES

The present work investigates the influence of pressure on the reaction timescales and NO_x emission of a premixed jet in vitiated crossflow. The present study attempts to fill a gap about axial-staged combustor knowledge, since a quantitative statement about the influence of pressure on NO_x emission has not been made in the open literature. The outcomes could be of high interest to further understand how applicable the data of flames at feasible laboratory pressure levels between 1atm and 5atm would be for burners at pressure levels 20atm to 30atm applied industrially. Patents in the field of axial-staged gas turbine combustion are owned by the OEMs Siemens [1, 2] and GE [3, 4].

On the experimental side, recent studies by [5] investigated a perfectly premixed research burner operated at high pressure levels between 8atm and 16atm. It was concluded that a pressure dependency of NO_x emission $X_{NO} \sim p^{const}$ can be formulated, but the constant would be temperature dependent. Higher pressure was shown to reduce both main stage burner NO_x and CO emission levels experimentally [5] with a pressure dependency in the range of $p^{0.5}$ for the main stage burner. Research by [6] focused on the influence of jet shape on the emission profiles of turbulent propane jet flames in crossflow. Experiments were conducted in a wind tunnel with an optically accessible test section attached. The upper and lower operating limits were screened by variation of the jet velocity. Lower CO emission and higher NO emission levels were the result of using elliptic jets relative to circular shaped jets [6]. A novel approach to obtain more reliable experimental NO_x emission monitoring was suggested by [7], describing a soft emission analyzer that utilizes an artificial neural network. Blowout limits of a methane jet diffusion flame surrounded by smaller fuel-flex jet pilot flames and air co-flow were studied experimentally by [8]. The

blowout limit was extended by increasing the pilot jet flow, allowing enhanced entrainment and higher thermal contribution of the side jets [8]. Flame hysteresis effects of methane jet flames with variable air co-flow were studied experimentally by [9] to determine characteristics of the instantaneous turbulent flame lift-off relative to the fuel velocity. Critical operating parameters of lean partially premixed methane-air turbulent combustion were investigated experimentally by [10] in a constant volume combustion chamber and visualized with a Schlieren shadowgraph. The effect of hydrogen enrichment, equivalence ratio, diluent addition, variation of injection pressure, chamber pressure, temperature and turbulence intensity were investigated. Addition of hydrogen was reported to be the critical parameter, allowing to improve the lean-burn limit of CH_4/air, improving peak p and T, and decreasing the duration of combustion cycles [10]. Utilization of process synergies and the integration of gasification into a combined cycle heavy duty gas turbine system were studied experimentally and numerically by [11]. Required adaptations of conventional combustors to allow operation with syngas include the combustor head and nozzle arrangements. Numerical results were verified with experimental data and a design was proposed for the mid and high pressure range.

Recent modeling efforts include a numerical LES investigation with *Star-CCM+* by [12] on the thermal uniformity and pressure drop of jet-in-crossflow mixing in a central swirler with staggered holes and various designs was able to document the axial and radial profiles with increased fidelity. The effects of distributed methane combustion on the temperature profile and thermal NO_x emission profile was investigated experimentally and numerically by [13]. The distribution profiles were adjusted with a swirl field and variation of the CH_4/air premix state under lean conditions. Outcomes improved the pattern factor

and achieved CO and NO_x emission levels in the low ppm range [13]. In a subsequent study by [14], the influence of premixed fuel/air dual injection in the swirl field was documented and found to further reduce emissions relative to the single injection pattern studied by [13]. A non-premixed turbulent jet flame (Sandia Flame D) was simulated with an experimentally verified Large Eddy Simulation (LES) by [15] to determine process irreversibilities and amount of entropy generation. Further numerical investigations by [16] covered the impact of nozzle configuration, such as the number and pattern of nozzles, use of premixed and non-premixed nozzles, and jet velocity by applying moderate or intense low-oxygen dilution (MILD) principles to an F class gas turbine combustor. Simulation at industrially relevant condition p = 16.3bar, air temperature of 723K and a lean equivalence ratio of 0.625 suggested a number of 12 nozzles and jet velocity 110m/s to be the optimal [16]. Simulations of an industrial gas turbine combustor were performed by [17] with gaseous CH_4 fuel under variation of the air flow distribution, recirculation and dilution characteristics to optimize for CO and NO_x emission. Thermal NO_x and prompt NO_x formation mechanisms were considered, and the results emphasized the strong dependency of thermal NO_x levels on the local firing temperature and amount of air dilution [17].

Studies by [18, 19] investigated the effect of pressure on hydrogen enriched natural gas jet flames in crossflow at pressure levels 10bar and 15bar to determine the axial flame stabilization mechanism. Earlier studies [20, 21] included qualitative emissions data under variation of the axial equivalence ratio and axial fuel split for axial-staged combustors and reheat combustors, but a trend of emission variation with pressure was not highlighted. A different experimental axial-staged combustion facility operating with a 0.8mm methane jet in vitiated hot crossflow at pressure levels between 5bar and 8bar was investigated by

[22]. Emission measurements were taken and axial NO_x addition with respect to the axial temperature rise was plotted at three pressure levels. However, a clear trend about the influence of pressure has not been determined, which could be justified with the pressure being varied between relatively high levels. The present study varies pressure level between 1atm and 5atm both experimentally and numerically. To extend the current knowledge to an axial combustion stage and isolate the known temperature dependency to a large extent, a constant centerline turbine inlet temperature level was targeted in this study and the mass flows scaled accordingly to account for the variation of pressure level. A trend was determined, and further understanding was sought for with a time scale analysis. Critical relation to model a combustion process is the turbulent Damköhler number *Da*, defined as the ratio between the turbulent (= mixing) time scale and the chemical time scale (eq. 1).

$$Da = \frac{\tau_{mix}}{\tau_{chem}} \tag{1}$$

τ_{mix} characterizes the local mixing time scale of the system as pre-defined in Star-CCM+ [23] according to eq. 2.

$$\tau_{mix} = (\beta^* * \omega)^{-1} \tag{2}$$

with β^* being a model constant defined at 0.09 and ω being the specific dissipation rate. τ_{chem} was defined as a custom function based on local CO_2 properties according to the *Star-CCM+* Steve Portal (eq. 3), an article based on [24, 25].

$$\begin{aligned}\tau_{chem} = [(\varepsilon + \$ProductionRateCO2) * \\ * (\varepsilon + \$MolecularWeightCO2)^{-1} * (\varepsilon + \$MolarConcentrationCO2)^{-1}]^{-1}\end{aligned} \tag{3}$$

τ_{chem} depends on the local CO_2 production rate, CO_2 molecular weight, local CO_2 molar concentration and a very small number ε to avoid definition errors (1e-12). The Damköhler number is used in this study to characterize the variation of the flame type depending on the system pressure. τ_{mix} is a moderate function of pressure, meanwhile τ_{chem} was shown to be strongly pressure dependent. A chemical activity profile for a 1D premixed laminar flame combustor and 250 dynamic grid points is shown in fig. 1. The significant differences of maximum heat release levels as well as streamwise length of heat release indicate the necessity for a 3D analysis for the relatively complex jet-in-crossflow field. The second objective of this paper was hereof defined to investigate the transition between shear layer burning at low pressure and a receded jet core flame at elevated pressure level using a timescale analysis.

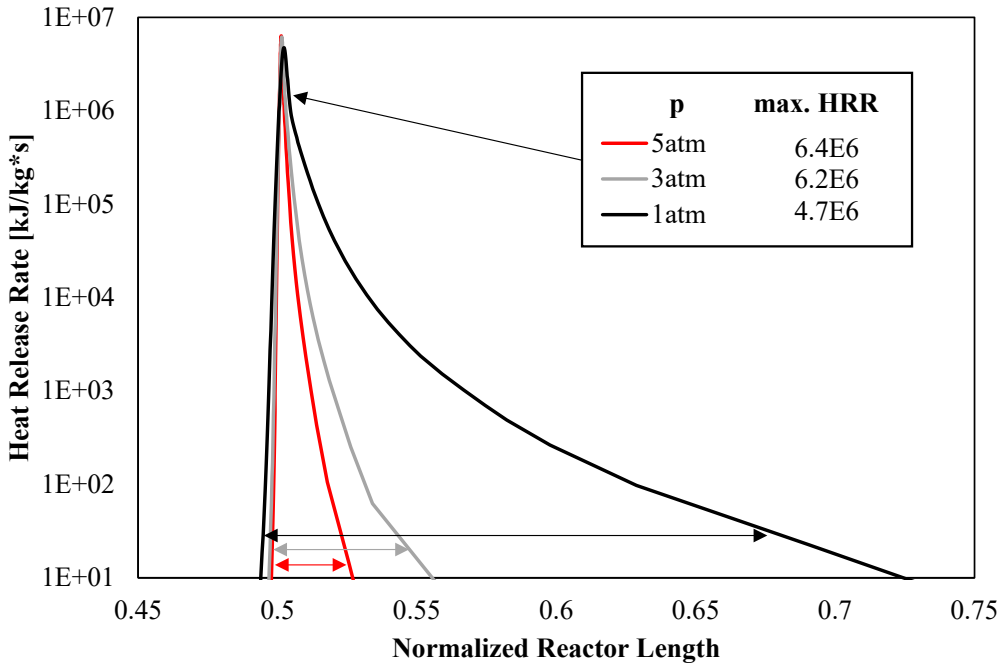

Figure 1: Chemical heat release of a 1D premixed laminar reactor simulated with dynamic grid points

2. EXPERIMENT AND DIAGNOSTICS

2.1 Combustor Configuration

The experimental facility is displayed in fig. 2. The facility consists of a main stage burner where a burner pipe houses a lean premixed methane-air mixture. A perforated screen is located between the main and axial stage to aid flow uniformity. The test section contains three optically accessible windows for imaging diagnostics, and an interchangeable top plate used to introduce fully premixed mixture to the facility in the second stage. The axial injector has an exit diameter of 12.7mm. At the downstream end of the facility, a choke plate with a diameter of 38.1mm is used to choke the flow to the desired pressure level. Further details about the experimental setup and procedure could be found in [26].

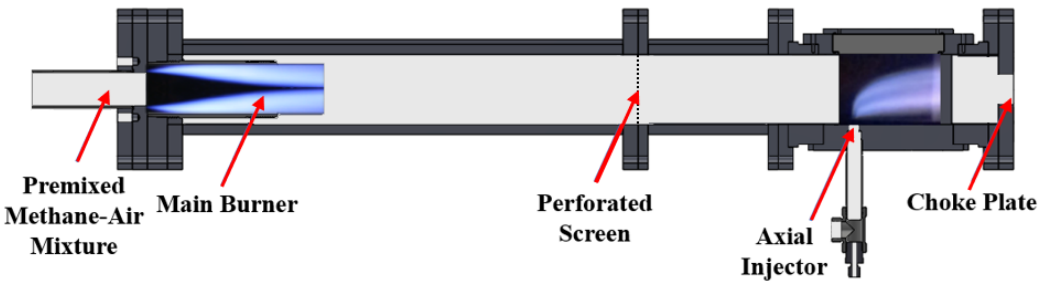

Figure 2: Experimental axially staged combustor test facility

At the exit of the choke pipe, a probe is placed in the center to capture exhaust gases for emissions measurements. The probe is large enough to capture a significant amount of gas to obtain a global average. Tests were done where the probe was traversed and the spatial location at the choke point did not have a significant effect on the measurements, confirming the obtained values accurately represent a global outlet average. The gases are carried through piping into a large ice bath to freeze any further reactions from occurring and condense out the water. A Horiba Mexa 584-L emissions analyzer was used to obtain

nitrogen oxide levels. Unless mentioned otherwise, emission levels in this paper are dry and corrected to 15% oxygen. In the CFD, the main stage boundary was defined using the measured data. The dilution average was taken by evaluating mass weighted surface average function one diameter after the jet penetrates. Outlet probe in the CFD was determined as a mass weighted surface average at similar position six jet diameters downstream of the choke plate. Referenced probe positions are shown in fig. 3.

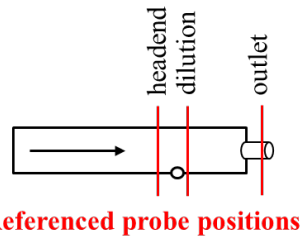

Figure 3: Species probe positions referenced numerically and experimentally

2.2 Data processing

Line of sight CH* chemiluminescence data at 200 microns per pixel spatial resolution was taken using a *Photron Fastcam SA1.1* at a rate of 125fps and a shutter speed of 1/1000; a narrowband 430 $\pm$ 2 nm filter was utilized to obtain CH* intensity. Since the CH* measured in the experiment corresponds to the chemiluminescent emission from CH species, the measured CH* concentration follows the CH concentration in the flame and a direct comparison with simulated CH species was deemed valid [27]. To replicate the experimental line-of-sight technique, simulated CH data was integrated along the z axis. A $\Delta y/d = 0.05$ was selected for the integration, weighting all z data equally. Accumulated sum of z and Δy data was normalized against the maximal area sum. Images were recorded with a resolution of 768x768 and were processed in *Matlab* to obtain time-averaged images considering one second worth of data for each testing condition. The flame boundaries are

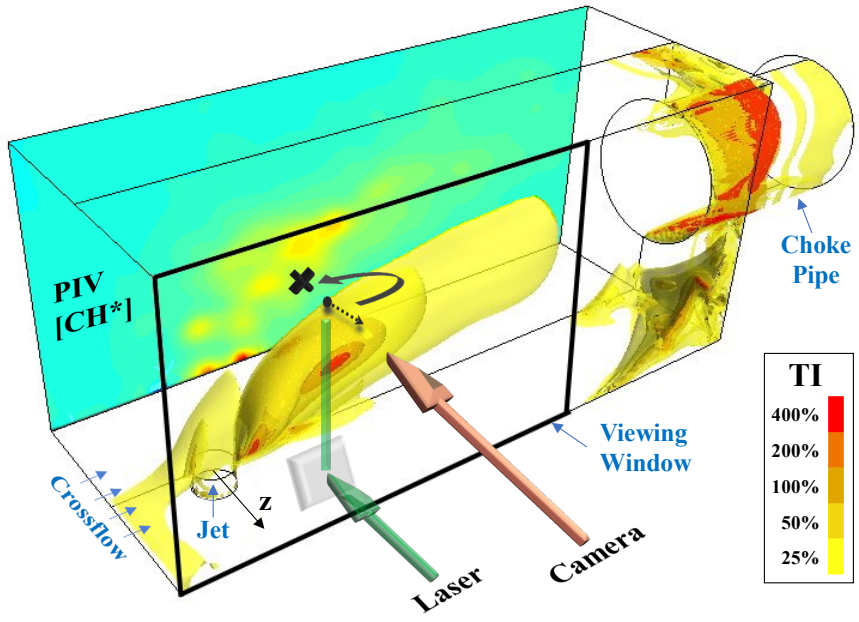

Figure 4: CFD integrative data processing to match experimental PIV and line-of-sight CH* chemiluminescence data

determined based on Otsu's threshold method [28]. Particle image velocimetry (PIV) was performed using a dual-head 532nm *Evergreen* laser with a time separation of 20µs. The PIV data is processed in PIVlab 2.00 using a contrast adaptive histogram equalization method (CLAHE). Figure 4 shows the overlay of planar turbulence intensity PIV data (blue plane) with simulated turbulence intensity (yellow-red 3D field), allowing an accurate representation of simulated data located at the z-symmetry plane.

3. STAR-CCM+ COMPUTATIONAL MODEL

3.1 Configuration Domain

Figure 5 shows the hexahedral, locally refined *Star-CCM+* mesh grid used to describe the axial stage of the in-house test rig with a dump region attached downstream. The 29 million cell mesh grid consists of two separate mesh continua, connecting the axial stage (1) with dimensions (x*y*z) = (195.1*88.9*38.1) mm to a choke pipe (l = 73mm, d

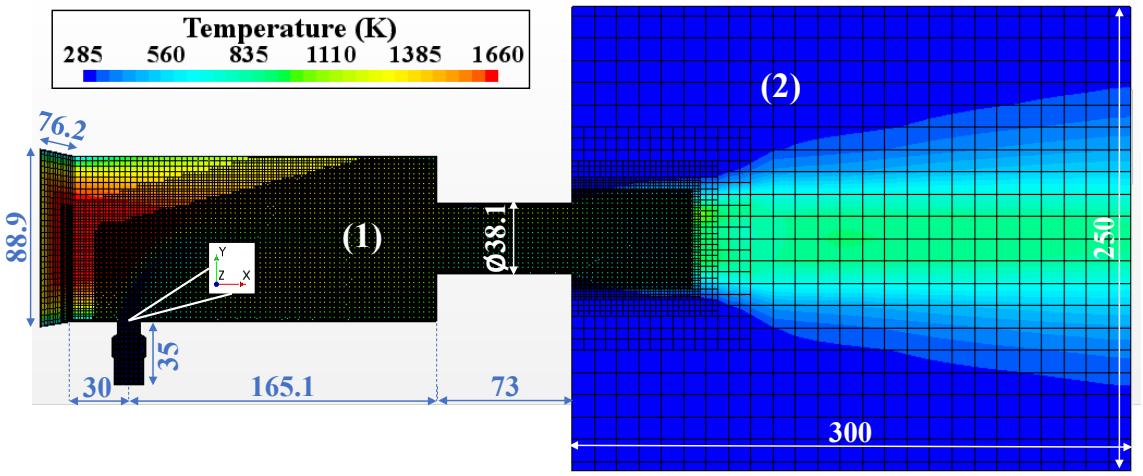

Figure 5: Axial stage and dump region dimensions and CFD mesh grid

= 38.1mm) and a dump region (2) linked with a conformal interface boundary. Grid convergence for the reacting jet trajectories, species reaction rates and temperature profiles was ensured for the refinement level Δs = 0.25mm. Position of local nitrogen oxide occurrence deviated for 19% with the 1mm grid and for 4% with the 0.5mm grid relative to the 0.25mm grid. Nitrogen oxide reaction rates deviated for 46% at 1mm and for 12% at 0.5mm relative to the 0.25mm grid. Hence, the latter resolution was used to refine the axial fuel line and combustion domain (1). A base size of 0.01m was selected for the dump zone cells with a stepwise transition to the combustor outlet cell size (Δs = 0.25mm). Symmetricity along the z-axis was utilized. Global origin of the coordinate system was defined at the collision point between crossflow and jet centerline as shown in fig. 5. Walls along the combustor and fuel line were defined at no-slip, smooth condition with the wall y^+ value set to 3 and wall heat transfer considered. Prism layer thickness was set to 0.4mm. The domain of interest is the viewing window made of fused silica with thermal conductivity k = 1.85W/mK at 700K and k = 1.4W/mK at ambient condition [29, 30], covering 90% of the inner rig contact area before x/d = 7. Using its thickness t = 25.4mm

and a temperature difference ΔT = 500K across the window walls yields a boundary heat flux of -32.5kW/m² (eq. 4).

$$\dot{q} = \frac{k}{s} * \Delta T = \frac{1.65 \frac{W}{mK}}{0.0254m} * 500K = 32.5 \frac{kW}{m^2} \quad (4)$$

The estimate is reasonable, given that steady state conditions are not reached due to rig run times being below 5 seconds paired with a strong main stage burner temperature profile. In addition, CFD and experimental data do not suggest any significant flame-wall interaction to occur along the windows [31]. Further downstream, 304 steel is the major wall component in use with a higher k = 20*W/mK* at 700K and k = 16*W/mK* at 300K [32, 33]. The jet walls were defined at constant T = 295K. The dump region (2) in fig. 5 is specified as a separate external flow zone. The plane surrounding the interface boundary was defined as an inlet at stagnating velocity and ambient condition. Boundaries downstream of that plane are defined as outlets at ambient pressure.

3.2 Reactive Flow Description

Building upon previous numerical and experimental studies with a 4mm axial jet [34-38], two *Star-CCM+* detailed chemistry models *Laminar Flame Concept* (LFC) and *Eddy Dissipation Concept* (EDC) were investigated for this study paired with the full GRI Mech 3.0 [39]. The species transport equation is defined as follows (eq. 5):

$$\frac{\partial}{\partial t}\rho Y_i + \frac{\partial}{\partial x_j}\left(\rho u_j Y_i + F_{k,j}\right) = \omega_i \quad (5)$$

with Y_k being the species mass fraction, ω_i being the species reaction source term and $F_{k,j}$ being the diffusion flux as a function of the turbulent Schmidt number. Both models consider the effect of turbulence on the combustion process implicitly through the

increased turbulent diffusivity provided by the turbulence model. For premixed turbulent flames, the diffusivity can be enhanced by reducing the turbulent Schmidt and Prandtl numbers, resulting in a turbulent flame speed and thickness that are greater than if the case were solely laminar. Detailed chemistry is solved for a *Constant Pressure Reactor* with a stiff ODE solver to integrate the chemical source terms, allowing a reaction system with a wide range of reaction time scales. The integration of chemical state is defined in eq. 6 with τ being the time step and r_k denoting the species reaction rate. [23, 40]

$$Y_i^* = Y_i + \int_0^\tau r_k\left(\mathbf{Y}, T, p\right) \mathrm{d}t \tag{6}$$

The right side of the species transport equation (eq. 5) defines the source term as a function of density ρ, mean reaction rate multiplier f, mass fraction and time step, shown in eq. 7:

$$\omega_i = \rho f\left(\frac{Y_i^* - Y_i}{\tau}\right) \tag{7}$$

For steady simulation with the *LFC*, the time scale is expressed by the residence time in the cell. The *LFC* (fig. 6 red line B) models the reacting jet-in-crossflow situation as an accelerated laminar flame with weak turbulence-chemistry interaction [23], hence f in eq. 7 is set to 1. Instantaneous reaction rate is evaluated for the mean temperature, pressure and species fraction. An early ignition at x/d = 2.5 was determined with the *LFC*. Reaction rates in the flame front were overpredicted by 2-3 orders of magnitude, resulting in a crescent flame shape and local CH concentration being consumed to all sides, even in the direction facing the main stage burner. The *Laminar Flame Concept* could be valid for premixed, partially premixed and unsteady flames [23], however it was not rated suitable

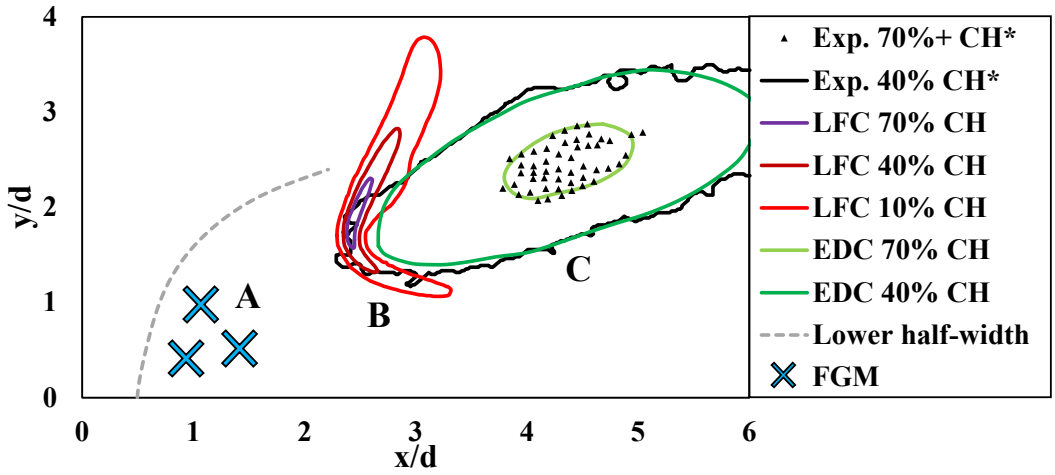

Figure 6: CFD jet-in-crossflow modeling at p=5atm: A: FGM, B: Laminar Flame Concept, C: Eddy Dissipation Concept

for this turbulence dominated, strongly finite-rate jet-in-crossflow flame configuration. Similarly, any Flamelet approach with tabulated GRI Mech 3.0 parameters would mispredict the flame position with an early lee-side ignition event, shown by the blue crosses (A) in fig. 6. The finite-rate *Eddy Dissipation Concept* (EDC) considers turbulence-chemistry interaction additionally in eq. 7 with a rate multiplier f < 1. The rate multiplier is defined in eq. 8.

$$f = \left(\left[C_l \left(\frac{\upsilon \tau_{turb}}{L^2} \right)^{0.25} \right]^{-3} - 1 \right)^{-1} \tag{8}$$

with C_l being the fine structure length constant, υ being the kinematic viscosity, τ_{turb} being the turbulent time scale and L being the turbulent length scale. Using the *EDC*, time step from eq. 7 is defined as follows (eq. 9):

$$\tau = F_{CFL}\, \tau_{turb} \tag{9}$$

with F_{CFL} being the CFL scaling factor. The *EDC* time-step is close to the smallest turbulent eddy (Kolmogorov) time scale; hence the effect of turbulence is modelled as a

reduction of the mean reaction rate relative to the *LFC* [23]. The *EDC* did a significantly better job describing the reactive zone, showing CH concentration (fig. 6 green lines (C)) in good agreement with the experimental data (black line). A slightly thicker CH flame front is followed by a broader domain of CH consumption, which is located solely downstream of the flame. Figure 6 shows the resulting overlay of CH concentration with the *Eddy Dissipation Concept* and the experimental verification with the CH* chemiluminescence data. Maximum CH levels are found between x/d = 4 and x/d = 5. The EDC fine structure factors were used at their default value. Turbulent Schmidt and Prandtl numbers were lowered from a default 0.7 to 0.5, which is in the range proposed by [41] to pronounce *RANS* turbulent momentum diffusion, follows the recommendation of [23, 40] for highly strained flows and was used for a similar axially staged configuration by [42]. The correction helped move the flame slightly back upstream and pronounce the spread of the radical domain as observed from the experimental CH* data. A slight underprediction of modelled horizontal CH spread has remained. The CFD simulation uses finite-rate chemistry to close the reaction rate, leveraging the full GRI-Mech 3.0 to provide species reaction rates and thermodynamic properties for the integration of finite kinetics. Use of a finite-rate chemistry model is in agreement with numerical investigations of [22] that used an axial-staged combustor at similar operating conditions. *EDC* simulated Damköhler numbers in the flame ranged up to 0.31 at pressure, this value was confirmed with calculated results, amounting up to 0.44 with a laminar flame speed of 7.1cm/s (determined with a 1D premixed laminar flame combustor and compared with literature data [43] for lean CH_4 combustion at p = 5atm) and turbulent fluctuations of 10m/s as determined from the PIV data (fig. 7).

The hot gas composition entering from the main burner was determined with an equilibrium calculation, using a constant pressure/enthalpy reactor. Equilibrium mass fractions of nine species CO, CO_2, H_2, H_2O, HO_2, N_2, O, O_2 and OH were complemented with measured NO and NO_2 main stage burner levels. Results for the main stage species boundary condition at p = 5atm are summarized in table 1. A weak pressure dependency was found for the equilibrium at lower pressure, main species remained near constant.

Table 1: Main stage burner species equilibrium calculation and measured NO_x data

φ_{main}	p [atm]	T_0 [K]	T_{equ} [K]	ρ_{equ} [kg/m^3]	Y_{CO}	Y_{CO2}	Y_{H2}
0.58	5	295	1733	0.98	9.0E-6	8.9E-2	/
Y_{H2O}	Y_{HO2}	Y_{N2}	Y_{NO}	Y_{NO2}	Y_O	Y_{OH}	Y_{O2}
8.7E-2	1.0E-6	7.4E-1	1.4E-5	2.0E-6	4.0E-6	1.6E-4	8.2E-2

3.3 Turbulent flow field

A coupled flow model with multi-component diffusion was required to account for the compressible flow field and the domain of choked flow. Material properties were determined with mass weighted mixture and Sutherland's Law method [40]. The *k-ω γ-Re$_\theta$ SST (Shear Stress Transport)* model was used and in relatively good agreement with the data. At the main stage outlet, a developing flow profile was determined for all pressure levels investigated. PIV velocity profiles are shown in fig. 7. At 1atm, the mass flows needed to be increased relative to the scaling law due to stability limits of the experimental high-pressure facility. Despite the increase of mas flow, the momentum flux ratio remained constant among the cases. Profiles at 3atm and 5atm were near-identical due to the linearly scaled condition.

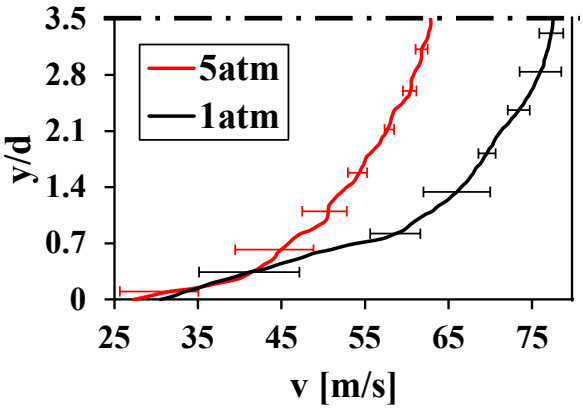

Figure 7: Averaged main stage PIV velocity profiles at pressure levels 5atm and 1atm

Maximum uncertainty was calculated to be 13% from the PIV data located in the near-wall domain. The measured main stage PIV profiles are reasonable, given the short entry length of x/d_h = 10 from the main stage inlets. Profiles in fig. 7 defined the CFD crossflow boundary condition and the γ-Re_θ transition function was defined to allow up to 25mm thickness of hydrodynamic boundary layer. An accurate description of the reacting jet trajectory was achieved and proven in previous work [36]. Crossflow turbulence intensity (TI) profile was determined from the PIV to rise from 15% at the centerline to about 30% along the wall. Turbulence intensity at the jet was set to 6% and turbulent length scales were set to L = 5mm at the main stage boundary and L = 1mm at the jet, respectively.

3.4 Grid convergence study

A grid convergence study was done by variation of the grid refinement in the critical jet and reactive domain between levels Δs = 0.25mm (29 million cells), Δs = 0.5mm (4.5 million cells) and Δs = 1.0mm (0.7 million cells). Target was to show the influence of coarser mesh size and to determine possible trade-offs that could be acceptable to mesh larger combustors for industry use. Figure 8 shows the CO_2 production rate plotted at iso-levels 1kg/m^{3}s, 10kg/m^{3}s and 20kg/m^{3}s.

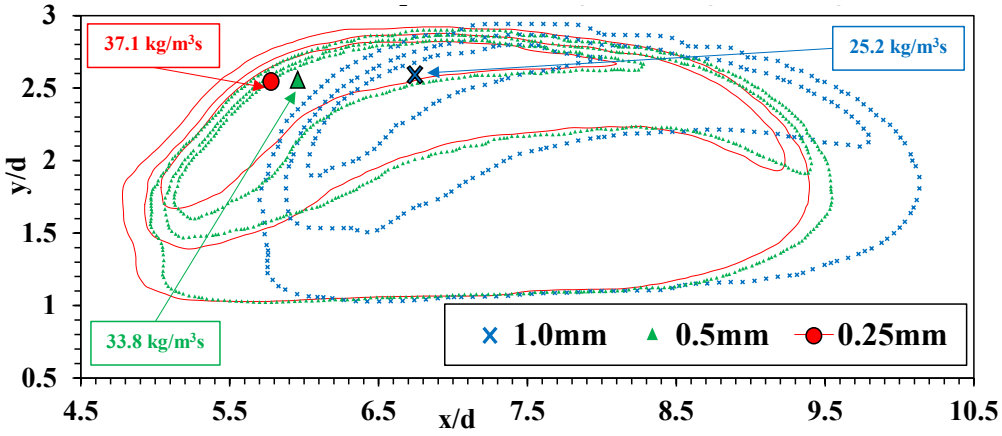

Figure 8: Production rate iso-levels 1kg/m^{3}s, 10kg/m^{3}s and 20kg/m^{3}s of CO_2 for three grid levels Δs = 0.25mm (red), 0.5mm (green) and 1.0mm (blue)

Whereas a sharp iso-levels contour at the upstream-most position was determined for the Δs = 0.25mm grid (fig. 8 red lines), some amount of numerical dissipation was recorded with the 0.5mm grid (fig. 8 blue crosses) and significant deviations were shown for the 1mm grid (fig. 8 green dots) in terms of the flame position and production levels. Details about the flame-CVP interaction are depicted less accurately upon transition to the coarser grids. Horizontal flame lift-off is strongly dependent on the mesh grid used and was shown to be 4% overpredicted for the 0.5mm grid and 19% overpredicted with the 1mm grid (relative to the 0.25mm grid). Vertical flame lift-off Δy was relatively unaffected. Maximum CO_2 production rate is strongly grid dependent, transition from Δs = 0.25mm to 0.5mm reduced the maximum rate by 9% and transition from 0.25mm to 1mm reduced the rate by 32%. End positions of significant CO_2 production were found to be 8% delayed for the 1mm grid and 2% delayed for the 0.5mm grid relative to the 0.25mm grid. A CentOS 7 cluster was used with Intel Xeon cores, x86_64 architecture with 28-32 cores per node and 128-192 GB RAM. A Lustre parallel file system with 56Gbit/s 4x FDR InfiniBand network fabric was used to transfer data. Power demand for a detailed chemistry simulation with 29 million cells was 20000 CPU hours at dampened under-relaxation factor settings.

3.5 Test Matrix

Mass flows were linearly scaled to operate at various pressure levels, keeping the fuel split, equivalence ratios and flow profiles near-constant. Influence of pressure reduction from 5atm to 3atm and 1atm was investigated with a lean $\varphi_{main} = 0.58$ and a lean premixed $\varphi_{Jet} = 0.75$ axial jet. The boundary conditions used to simulate the investigated operating points are stated in table 2.

Table 2: Test Matrix with a 12.7mm lean premixed axial jet at three pressure levels

Main Burner Stage					**Axial Stage**				
$\dot{m}_{main}^{CH4}$ [g/s]	$\dot{m}_{main}^{air}$ [g/s]	φ_{main} [-]	**Centerline**		$\dot{m}_{Jet}^{CH4}$ [g/s]	$\dot{m}_{Jet}^{air}$ [g/s]	φ_{Jet} [-]	T_{Jet} [K]	p [atm]
			T_{main} [K]	v_{main} [m/s]					
14.46	430.6	0.58	1610	62	2.52	48.7	0.75	290	5
8.65	213.1			64	1.51	29.2			3
4.57	112.5			80	0.80	15.4			1

4. RESULTS AND DISCUSSION

4.1 Nitrogen Oxide Emission

A comparison of the simulated and experimental NO levels determined at the choke pipe outlet position (as described in section 2.1) are summarized in table 3.

Table 3: Corrected Nitrogen Oxide Emission with a lean premixed 12.7mm axial jet

φ_{main} [-]	φ_{Jet} [-]	p [atm]	$NO_{main,Exp.}$ [ppm]	$NO_{outlet,Exp.}$ [ppm]	$NO_{outlet,CFD}$ [ppm]
0.58	0.75	5	5.0	5.5	5.9
		3	4.0	8.0	8.8
		1	2.5	14.0	15.5

Trend for the main burner nitric oxide (NO) levels is in agreement with [5, 44] and was determined to scale with $p^{0.4}$. Global NO outlet emission was found to scale with $p^{-0.55}$ for both the CFD and experimental data (eq. 10). A global definition in equation form was stated by using the NO emission level at 1atm as a reference point (fig. 9). Elevated pressures allow an axial NO_x benefit due to the reduced axial flame surface and higher amount of axial burning in the jet core (cf. section 4.2).

$$X_{NO,global} = f(p^{-0.55}) \tag{10}$$

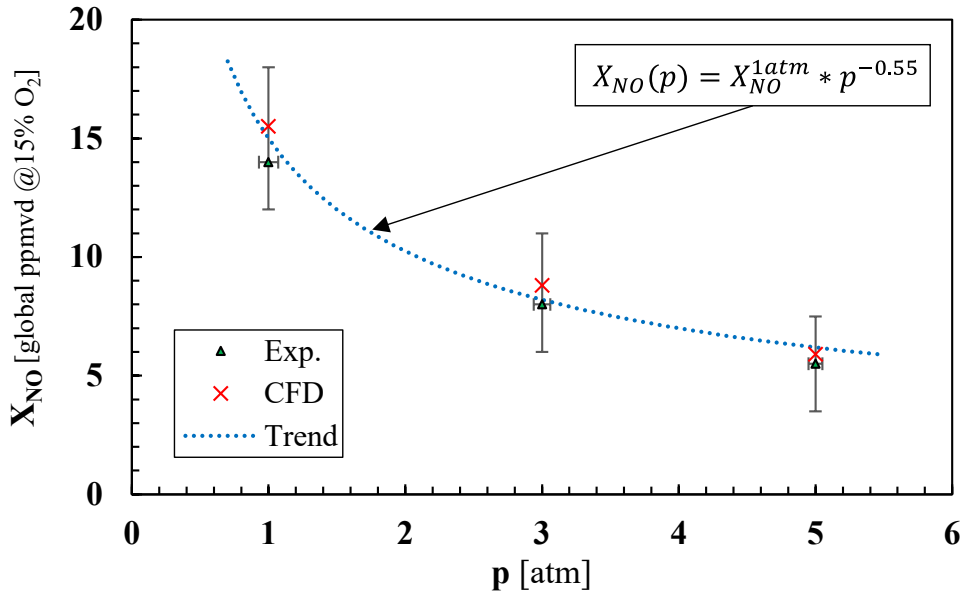

Figure 9: Pressure dependency of global NO emission at T_{outlet} = 1700K

Experimental pressure measurement was relatively accurate with a deviation of ±25kPa at pressure and ±35kPa at atmospheric condition. Accuracy of the experimental NO measurement was limited by the accuracy of the gas analyzer; increased positive emission uncertainty was stated for the experimental 1atm condition since the combustion event may have been just near complete in the given facility length. Measured outlet UHC levels remained low (3ppm).

4.2 Local flame and nitrogen oxide occurrence

Influence of pressure reduction from 5atm to 1atm on the reaction timescale and local NO levels was investigated in fig. 10A and 10B. To characterize the flame, CFD data for the molar concentration of CH was processed by evaluating line integrals along the z direction at x/d = 5 (fig. 10C). Uncertainty of CH* signal (figs. 10C and 11C) ranged up to $I/I_{max} = \pm 0.1$ due to turbulent fluctuations of the flame and flow field. To obtain the correct result for the x/d plane (fig. 10C), a $\Delta y = 0.05$ was selected and all z values in the increment added up and normalized with respect to the sum at the maximum concentration level (cf. section 2.2). Figure 10 (p = 5atm (A), p = 1atm (B)) plots normalized CH and NO mole fraction data along y and z at a position x/d = 5 downstream of the jet. The 5atm core flame

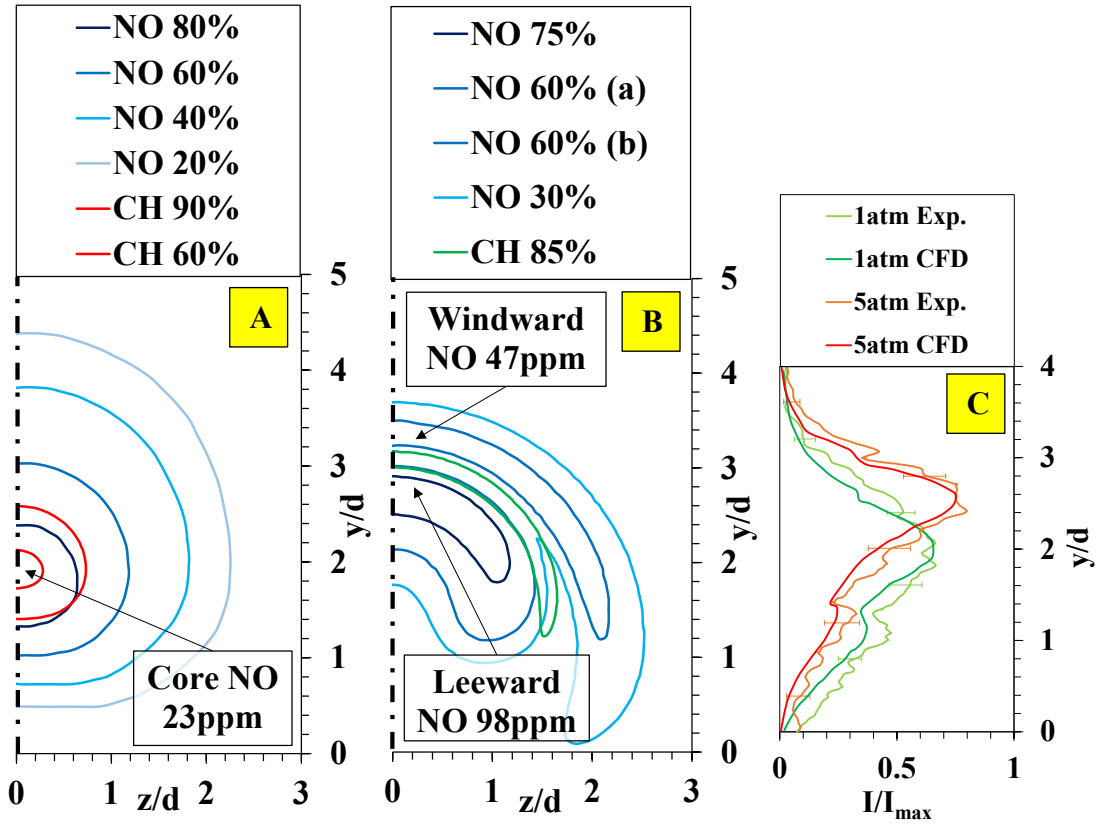

Figure 10: $\varphi_{main} = 0.58$, $\varphi_{Jet} = 0.75$, position x/d=5: CH and NO concentration (CFD) along the y,z directions: p=5atm (A) and p=1atm (B); CH* (experimental) and CH (z-integrated CFD) along the y direction (C)

shows NO production levels (blue lines) in spatial agreement with the CH levels (red line). Maximum NO level in the core is 23ppm and pronounced spread is found at the windward side due to proximity of the hot crossflow. At 1atm, the near-flame domain (green line) separates two branches of NO occurrence (blue lines). Maximum NO level of 98ppm can be found at the leeward side, indicating that convective transport at the *CVP* center is not enough to entirely inhibit NO levels accumulating in the domain between the flame front and the vortex center. Figure 10 (C) shows the verification of z-integrated CH from the CFD with experimental CH* chemiluminescence data at the position x/d = 5, plotting the y/d axis against the normalized intensity level. Both CFD flames show CH levels in a domain between y/d = 0 and y/d = 4 and follow the measured data with deviations below 20%. Maximum z-accumulated CH intensity can be found at y/d = 2 for the shear layer flame (p = 1atm), denoted by the green line in fig. 10 (C). At p = 5atm, the red line (fig. 10 C) represents a higher maximum CH level for the core flame, found at y/d = 2.5. At x/d = 5 (fig. 10 A), the p = 5atm data show a core flame burning close to the symmetry plane, exhibiting minor changes in the CH profile by contribution of the z data. The line integration method described above was particularly critical to match the p = 1atm flame (fig. 9 B), considering shear layer burning with a contribution of simulated CH signals up to two jet diameters off the symmetry plane.

A similar analysis from a top view (at constant position y/d = 2) is depicted in fig. 11. Compared were simulated CH and experimental CH* chemiluminescence data at p = 5atm (A) and p = 1atm (B) as well as the z-integrated CH signal for verification (C). At p = 5atm, the CH tailing phenomenon shown in fig. 11C can be tracked in the x,z-space: figure 11A shows decaying NO levels towards the outlet. This behavior suggests produced

NO to be either transported to higher y/d positions by the *CVP,* or to be further oxidized to NO_2 in the low temperature domain facing the bottom wall. The p = 1atm data (fig. 11B) validate statements made for fig. 10. The top view of the two NO branches is shown to be separated by the shear layer flame front. NO levels trapped at the inside of the *CVP* reach peak levels of 67ppm. A less steep slope with lower maximum intensity at x/d = 6 proves the slower reaction progress in the shear layer. CH levels were fully consumed before x/d = 7 (fig. 11C light green), this behavior was verified with the CFD (fig. 11C dark green).

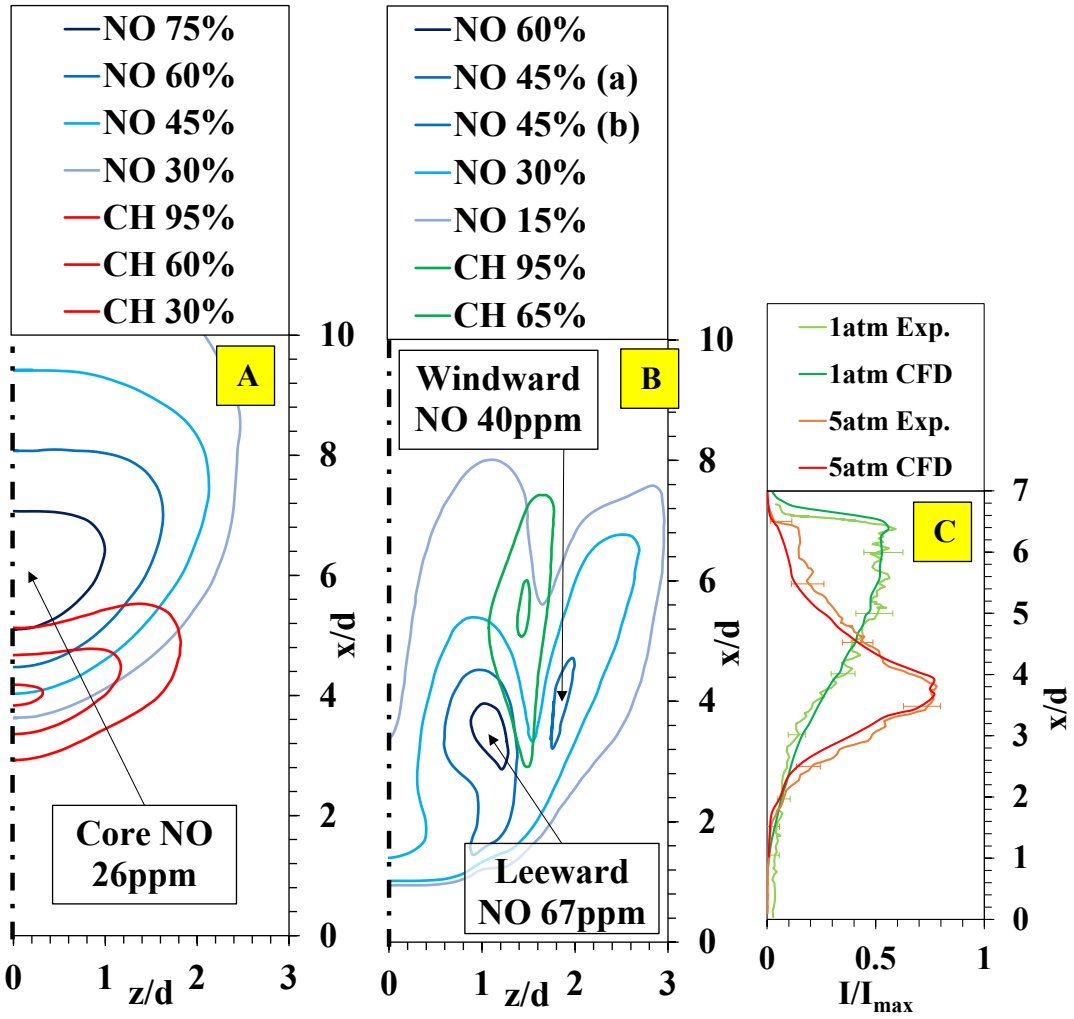

Figure 11: φ_{main} = 0.58, φ_{Jet} = 0.75: CH and NO concentration (CFD) along the x,z directions: p=5atm (left) and p=1atm (center); CH* (experimental) and CH (z-integrated CFD) along the x direction (right)

A comparison of the 5atm and 1atm total peak areas in figs. 10 and 11 indicate that similar total CH amounts are present throughout the plane, the z-data revealed that local distribution plays a significant role for the emissions results. Based on the data analyzed, pressure is seen to aid with lowering the production of NO_x emissions in the axial stage as a result of the occurring flame stabilization mechanism. Experimental data underlines the significant influence of pressure on emission levels. At p = 5atm, 5.0ppm NO at 15% oxygen was measured after the main stage and 5.5ppm at the axial stage outlet. In contrast, at atmospheric pressure, 2.5ppm was determined after the main stage and 14ppm at the axial outlet. The concept of axial staging is relatively ineffective at low pressure but significant emission saving potential was proven at lab-scale high pressure level 5atm.

4.3 Turbulence Intensity

To get a certain amount of insight to the turbulent scales, simulated and experimental turbulence intensities at the lee-side recirculation zone (x/d = 2.5) are compared in fig. 12. Experimental PIV data were time-averaged and filtered to obtain relatively smooth turbulence intensity profiles with maximum errors of 20% (fig. 12 A). A significant pressure dependency of local turbulence intensities at the jet lee-side was determined. Maximum intensity levels at a position y/d = 1.7 were found to be 60% at 5atm, 75% at 3atm and 115% at atmospheric condition. Beyond the windward trajectory edge, turbulence intensity shows a weak pressure dependency within levels of 20% and 25% (fig. 12 A), these levels were found in the CFD as well. Figure 12 B shows the simulated y,z field of turbulence intensity 50% iso-levels at the similar position x/d = 2.5. The CFD trend shows a more pronounced recirculation zone at lower pressure level. Since the PIV technique is well focused on the centerline by using a collimated laser sheet, the centerline axis (z = 0)

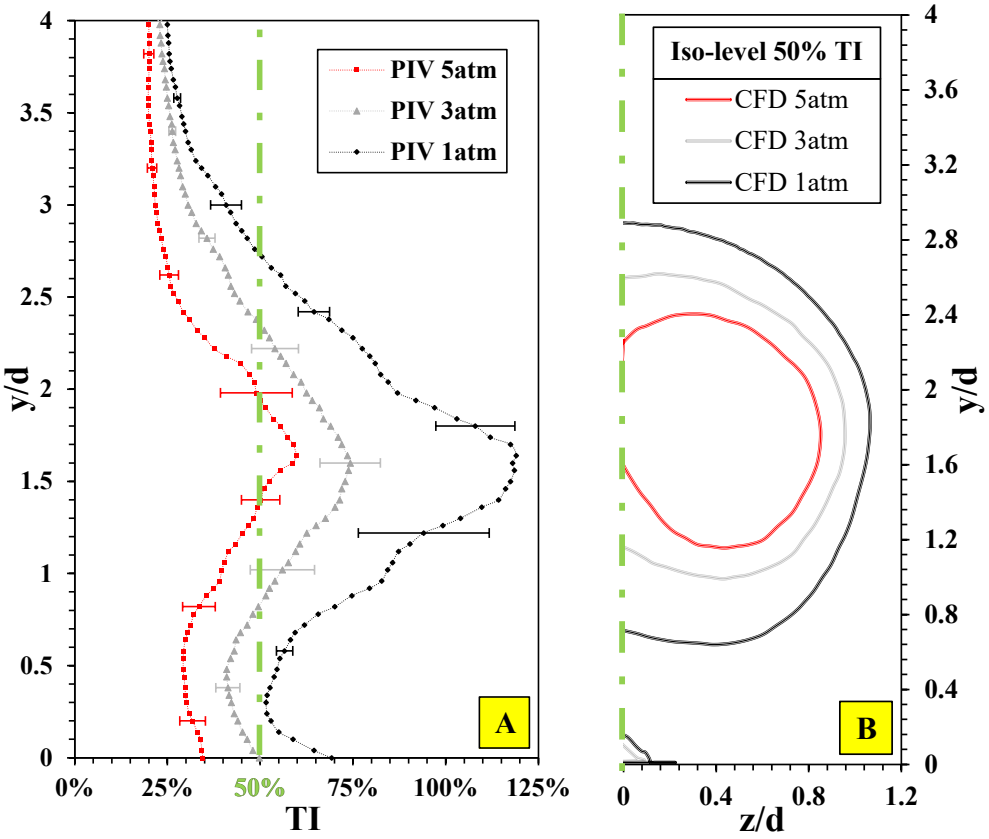

Figure 12: Turbulence intensities in the recirculation zone at three pressure levels. A: Filtered PIV data. B: Perpendicular y,z plane with 50% TI iso-level from the CFD

of simulated 50% iso-level can be used for comparison with the profile found at a TI level of 50% in the PIV data. Evaluated position for this perpendicular comparison is highlighted with the green dashed lines in figs. 12 A and 12 B. The line profiles are relatively similar and suggest the RANS *k-ω γ-Reθ SST* model with intensity and dissipation boundary conditions defined in section 3.3 to give a good approximate description of the turbulent scales and their variation with system pressure.

4.4 Timescale Comparison

Analysis of the present time scales at different pressure levels is described in this section. Averaged trends of the Damköhler number throughout the combustor are investigated in fig. 13.

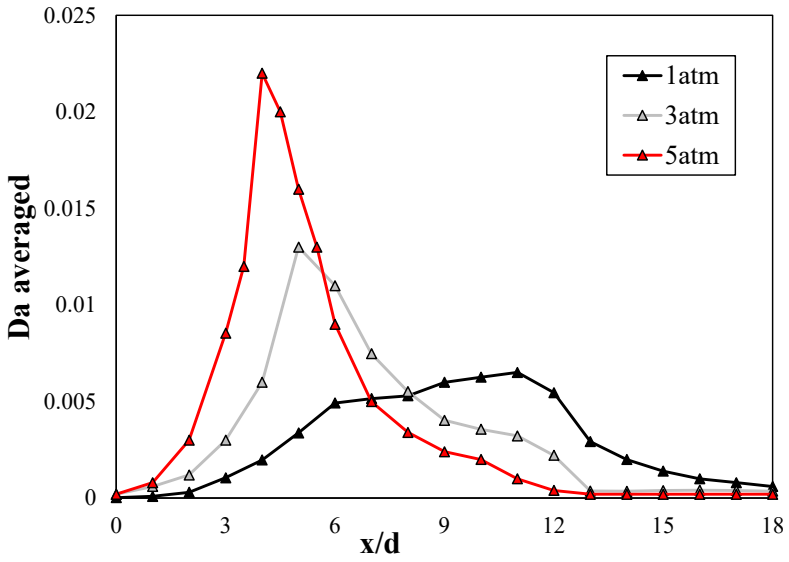

Figure 13: Averaged Damköhler number at three pressure levels along the axial stage

Mass weighted *y,z* surface average of the Damköhler number was evaluated with an increment of x/d = 1. For the p = 5atm condition, average was evaluated with an increment x/d = 0.5 to capture the steep rise of *Da* at the flame. At p = 5atm, a distinct maximum was recorded with a certain amount of tailing towards the combustor outlet. At p = 3atm, the similar trend was found but dampened due to the lower operating pressure. In contrast, a significant deviation is shown at atmospheric pressure. Combustion event is delayed, and maximum Damköhler number is reached after x/d = 10.

Due to the occurrence of local combustion event along the jet shear layer (particularly at low pressure), further analysis is required to quantitatively compare Damköhler numbers. Figure 14 shows the y and z directions at two distinct positions x/d = 5 and 10 downstream of the axial jet. At p = 5atm, elevated local Damköhler number Da = 0.31 was found after x/d = 5 at the flame, located at the windward trajectory edge. A certain amount of jet core burning was recorded as shown by the relatively wide reactive domain. Combustion is near-complete at x/d = 10, production of post-flame NO remains as a weak

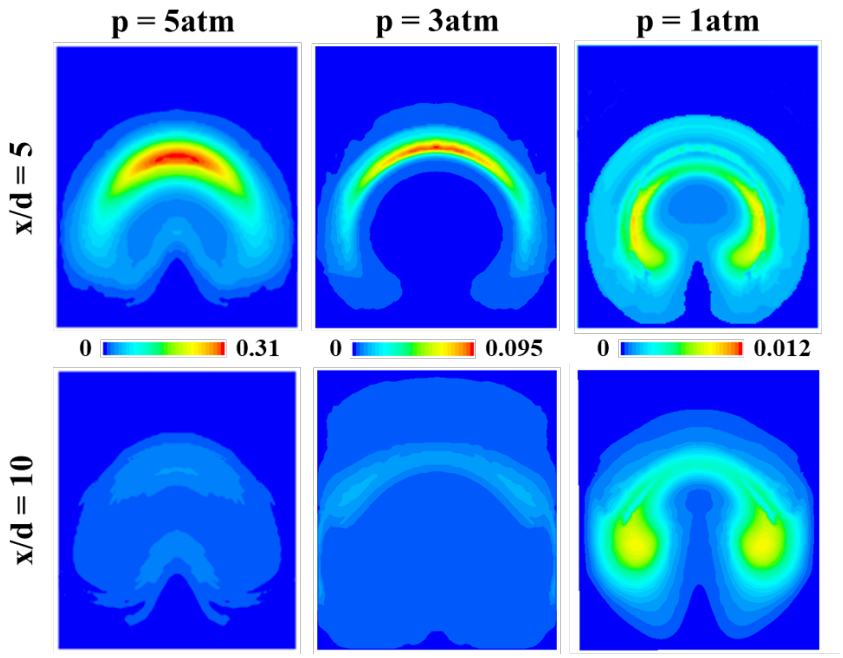

Figure 14: Local Damköhler number at three pressure levels and two positions downstream of the axial jet

signal. At p = 3atm, maximum local Damköhler number Da = 0.095 is found at the windward edge. Reactions take place in a thinner domain at p = 3atm (fig. 14) that surrounds the jet more. Similarly, reaction is relatively complete at x/d = 10. Pressure reduction to p = 1atm shows a significantly lower Da = 0.012 and distinct change in the reaction kinetics. Shear layer burning is concentrated in the *CVP*, the flame may interact locally with the vortex center. At p = 1atm, reaction progress is slow and significant reaction activity is present at x/d = 10. Applying the gained knowledge with the analysis in sections 4.1 and 4.2, the reason for high NO formation at low pressure can be tracked in fig. 14. Due to the reduced bimolecular collision rate as a function of $Da \sim p^2$, a longer (x/d direction) flame with more radial surface area (y/d, z/d) produces more radicals and favors elevated NO production. In contrast, at p = 5atm, a relatively short, receded jet core flame is located at the windward trajectory side, allowing a significantly smaller flame surface and reduced NO levels, despite the locally higher temperature level.

5. CONCLUSION

This paper investigates lean premixed 12.7mm axial jets in vitiated crossflow with detailed chemistry and 53 species considered. All operating points were validated against in-house experimental data and found to be in the finite rate regime. Simulated exit nitrogen oxide levels were validated with experimental emission data and a global emission trend for the pressure dependency of corrected nitrogen oxide emission was found to be $X_{NO,global} = f(p^{-0.55})$ for the investigated turbine inlet temperature level T = 1700K. A substantial difference about the reaction kinetics and local nitrogen oxide production was pointed out for the pressure dependent transition between two flame types. At elevated pressure of 5atm, jet core burning was determined at relatively high Damköhler number of 0.3. A receded core flame with a compact flame surface produced a moderate amount of NO emission along the jet core. High windward thermal NO emission was avoided due to the moderate temperature level used in this study. At atmospheric pressure, prolonged shear layer burning at low Da = 0.015 was determined to cause the elevated amount of nitrogen oxide emission. The physical reason was tracked with an analysis of the reaction time scale. The flame surrounded the entire shear layer and combustion required twice the axial length relative to combustion at pressure. Result was a large flame surface and high accumulation of NO at both sides of the shear layer. A $Da \sim p^2$ dependency of the local Damköhler number was determined for the transition between shear layer burning and jet core burning. Chemical timescales were shown to match with experimental data by an analysis of the CH* chemiluminescence signal and simulated CH concentration in the flame. In contrast, a moderate pressure dependency was determined for the contribution of the turbulent timescales. Higher turbulence intensity along the lee-side recirculation zone

of the jet at lower pressure was shown with an overlay of the PIV data and simulated turbulence intensities.

ACKNOWLEDGMENTS

The authors (BS, TG, MO, KA and SM) acknowledge support from the Department of Energy under Award Number DE-FE0031227 and collaboration with Dr. Carlos Velez and GE Global Research.

NOMENCLATURE

d	jet diameter, m
Da	Damköhler number

J	momentum flux ratio
k	thermal conductivity, W/mK
L	turbulent length scale, m
l	length, m
$\dot{m}$	mass flow rate, kg/s
p	pressure, atm
$\dot{q}$	heat flux, W/m^2
s	cell dimension, m
T	temperature, K; °C
t	thickness, m
u	velocity, m/s
$\dot{w}$	reaction rate, g/m^{3}s
X	mole fraction
x	axial coordinate, downstream position, m
Y	mass fraction
y	perpendicular coordinate, penetration depth, m
y^+	wall criterion
z	lateral coordinate, m

Greek Letters

γ-Re_θ	Transition model
Δ	difference
ε	turbulent dissipation rate
φ	equivalence ratio
ρ	density
τ	time scale
ω	turbulent dissipation rate
ω	vorticity

Subscripts and superscripts

axial	axial stage
chem	chemical
exp	experimentally measured
global	entire combustor
jet	axial jet
main	main burner stage
max	maximum
turb	turbulent

Acronyms and abbreviations

CFD	Computational Fluid Dynamics
CVP	Counter Rotating Vortex Pair
EDC	Eddy Dissipation Concept
fps	frames per second
JiC	Jet-in-Crossflow
LES	Large Eddy Simulation
LFC	Laminar Flame Concept
PIV	Particle Image Velocimetry
ppmvd	parts per million on volumetric, dry basis
RANS	Reynolds Averaged Navier Stokes
RST	Reynolds Stress Turbulence
SST	Shear Stress Transport
UHC	Unburned Hydrocarbons

REFERENCES

[1] Laster, W. R., Martin, S. M., Bilbao, J. E. P., Hardes, J., Fox, T. A., 2018, "Dual Outlet Nozzle for a Secondary Fuel Stage of a Combustor of a Gas Turbine Engine," Patent US 10,139,111 B2, Siemens Energy, Inc.

[2] Martin, S. M., Cai, W., Harris, J., 2013, "Apparatus and Method for Controlling the Secondary Injection of Fuel," Patent US 8,387,398 B2, Siemens Energy, Inc.

[3] Venkataraman, K. K., Washam, R. M., Karim, H., Terry, J. C., Davis, L. B., 2014, "Late Lean Injection System Configuration," Patent US 8,701,383 B2, General Electric Company.

[4] Venkataraman, K. K., Terry, J. C., Velkur, C. B., Karim, H., 2014, "Late Lean Injection Fuel Staging Configurations," Patent US 8,707,707 B2, General Electric Company.

[5] Elkady, A. M., Herbon, J., Kalitan, D. M., Leonard, G., Akula, R., Karim, H., Hadley, M., 2012, "Gas Turbine Emission Characteristics in Perfectly Premixed Combustion," J. Eng. Gas Turbines Power, 134, p. 061501.

[6] Gollahalli, S. R., Pardiwalla, D., 2002, "Comparison of the Flame Characteristics of Turbulent Circular and Elliptic Jets in a Crossflow," Journal of Energy Resources Technology, 124, pp. 197-203.

[7] Al-Malak, A., Elshafei, M., Habib, M. A., Al-Zaharnah, I., 2016, "Soft Analyzer for Monitoring NOx Emissions From a Gas Turbine Combustor," Journal of Energy Resources Technology, 138, p. 031101.

[8] Kibrya, M. G., Karim, G. A., 1996, "Kibrya, M. G., & Karim, G. A. (1996). Blowout Limits of a Jet Diffusion Flame in the Presence of Small Surrounding Jet Pilot Flamesdoi:10.1115/1.2792705 " Journal of Energy Resources Technology, 118, pp. 140-144.

[9] Moore, N. J., Terry, S. D., Lyons, K. M., 2011, "Flame Hysteresis Effects in Methane Jet Flames in Air-Coflow," Journal of Energy Resources Technology, 133, p. 022202.

[10] Askari, O., Metghalchi, H., Hannani, S. K., Hemmati, H., Ebrahimi, R., 2014, "Lean Partially Premixed Combustion Investigation of Methane Direct-Injection Under Different Characteristic Parameters," journal of Energy Resources Technology, 136, p. 022202.

[11] Liu, S., Yin, H., Xiong, Y., Xiao, X., 2017, "A Comparative Analysis of Single Nozzle and Multiple Nozzles Arrangements for Syngas Combustion in Heavy Duty Gas Turbine," Journal of Energy Resources Technology, 139, p. 022004.

[12] Elgammal, T., Amano, R. S., 2018, "Effectiveness of Central Swirlers in the Thermal Uniformity of Jet-in-Crossflow Mixing," Journal of Energy Resources Technology, 140, p. 101202.

[13] Khalil, A. E. E., Gupta, A. K., Bryden, K. M., Lee, S. C., 2012, "Mixture Preparation Effects on Distributed Combustion for Gas Turbine Applications," Journal of Energy Resources Technology, 134, p. 032201.

[14] Khalil, A. E. E., Gupta, A. K., 2014, "Dual Injection Distributed Combustion for Gas Turbine Application," Journal of Energy Resources Technology, 136, p. 011601.

[15] Safari, M., Sheikhi, M. R. H., 2014, "Large Eddy Simulation for Prediction of Entropy Generation in a Nonpremixed Turbulent Jet Flame," Journal of Energy Resources Technology, 136, p. 022002.

[16] Deng, X., Xiong, Y., Yin, H., Gao, Q., 2016, "Numerical Study of the Effect of Nozzle Configurations on Characteristics of MILD Combustion for Gas Turbine Application," Journal of Energy Resources Technology, 138, p. 042212.

[17] Emami, M. D., Shahbazian, H., Sunden, B., 2019, "Effect of Operational Parameters on Combustion and Emissions in an Industrial Gas Turbine Combustor," Journal of Energy Resources Technology, 141, p. 012202.

[18] Saini, P., Chterev, I., Pareja, J., Aigner, M., Boxx, I., 2020, "Effect of Pressure on Hydrogen Enriched Natural Gas Jet Flames in Crossflow," Flow, Turbulence and Combustion, pp. 1-20.

[19] Fleck, J. M., Griebel, P., Steinberg, A. M., Arndt, C. M., Aigner, M., 2013, "Auto-ignition and flame stabilization of hydrogen/natural gas/nitrogen jets in a vitiated cross-flow at elevated pressure," International Journal of Hydrogen Energy, 38, pp. 16441-16452.

[20] Fleck, J. M., Griebel, P., Steinberg, A. M., Stöhr, M., Aigner, M., 2010, "Experimental imvestigation of a generic, fuel flexible reheat combustor at gas turbine relevant operating condition," Proceedings of ASME Turbo Expo.

[21] Lückerath, R., 2015, "HTV-EB Robustes Hochtemperaturverbrennungssystem mit erweitertem Betriebsbereich," Schlussbericht, Teile I + II.

[22] Prathap, C., Galeazzo, F. C. C., Kasabov, P., Habisreuther, P., Zarzalis, N., Beck, C., Krebs, W., Wegner, B., 2012, "Analysis of NOx Formation in an Axially Staged Combustion System at Elevated Pressure Conditions," J. Eng. Gas Turbines Power, 134(3).

[23] Simcenter STAR-CCM+® Documentation User Guide Version 14.04, 2019, © Siemens PLM Software.

[24] Poinsot, T., Vernante, D., 2005, Theoretical and Numerical Combustion Second Edition, ©2004 Book News, Inc., Portland, OR.

[25] Borghi, R., 1985, "On the structure and morphology of turbulent premixed flames," Recent advances in the Aerospace Sciences, pp. 117-138.

[26] Genova, T., Otero, M., Ahmed K.A., 2020, "Partial Premixing Effects on the Reacting Jet of a High Pressure Axially Staged Combustor," Journal of Engineering for Gas Turbines and Power.

[27] Nori, V. N., Seitzman, J. M., 2009, "CH* chemiluminescence modeling for combustion diagnostics," Proceedings of the Combustion Institute, 32, pp. 895–903.

[28] Yan, W., Wang, C., Guo, J., 2012, "One Extended OTSU flame Image recognition Method Using RGBL and Stripe segmentation " Applied Mechanics and Materials, 121-126, pp. 2141-2145.

[29] Combis, P., Cormont, P., Gallais, L., Hebert, D., Robin, L., Rullier, J.-L., 2012, "Evaluation of the fused silica thermal conductivity by comparing infrared thermometry measurements with two-dimensional simulations," Applied Physics Letters, 101, p. 211908.

[30] Wray, K. L., Connolly, T. J., 1959, "Thermal Conductivity of Clear Fused Silica at High Temperatures," Journal of Applied Physics, doi: 10.1063/1.1735040, 30, pp. 1702-1705.

[31] Poinsot, T., Gicquel, L., Cuenot, B., Staffelbach, G., Vermorel, O., Wolf, P., Boileau, M., Colin, O., Veynante, D., Selle, L., Sensiau, C., Benoit, L., Gullaud, E., Berat, C., Moureau, V., 2013, "Flame / wall interactions in combustion chambers," IMF Toulouse, CNRS and INPT, CERFACS Report.

[32] Harvey, P. D., 1982, Engineering Properties of Steels, American Society for Metals.

[33] Peckner, D., Bernstein, I. M., Peckner, D., 1977, "Handbook of Stainless Steels, New York: McGraw-Hill," McGraw-Hill Book Company.

[34] Stiehl, B., Worbington, T., Miegel, A., Martin, S., Velez, C., Ahmed, K., 2019, "Combustion and Emission Characteristics of a Lean Axial-Stage Combustor," Proceedings of ASME TurboExpo 2019.

[35] Stiehl, B., Worbington, T., Woodard, A., Ahmed, K., 2020, "Numerical Simulation of an Axial-Staged Combustor at High Pressure," 2020 AIAA SciTech Forum and Exposition.

[36] Stiehl, B., Otero, M., Genova, T., Worbington, T., Reyes, J., Ahmed, K., Martin, S., Velez, C., 2021, "Simulation of Premixed and Partially Premixed Jet-in-Crossflow Flames at High-Pressure," Journal of Engineering for Gas Turbines and Power.

[37] Genova, T., Otero, M., Stiehl, B., Reyes, J., Ahmed, K., Martin, S., 2019, "Exploration of a Reacting Jet-in-Crossflow in a High-Pressure Axial Stage Combustor," AIAA Propulsion and Energy 2019 Forum.

[38] Otero, M., Genova, T., Reyes, J., Stiehl, B., Ahmed, K., Martin, S., 2019, "Characteristics of a Reacting Jet-in-Crossflow at Elevated Pressures," AIAA Propulsion and Energy 2019 Forum.

[39] Smith, G. P., Golden, D. M., Frenklach, M., Moriarty, N. W., Eiteneer, B., Goldenberg, M., Bowman, C. T., Hanson, R. K., Song, S., Gardiner, Jr., W. C. Lissianski, V. V. and Qin, Z., "GRI-MECH 3.0," http://www.me.berkeley.edu/gri_mech/.

[40] Karalus, M., 2019, "Best Practices for RANS Combustion."

[41] Tominagaa, Y., Stathopoulos, T., 2007, "Turbulent Schmidt numbers for CFD analysis with various types of flowfield," Atmospheric Environment, 41, pp. 8091-8099.

[42] Loparo, Z., 2015, "Validation of CFD models of a second-stage combustion system using STAR-CCM+," UTSR Internship Report University of Central Florida.

[43] Amirante, R., Distaso, E., Tamburrano, P., Reitz, R. D., 2017, "Laminar flame speed correlations for methane, ethane, propane and their mixtures, and natural gas and gasoline for spark-ignition engine simulations," International Journal of Engine Research, 18(9), pp. 951-970.

[44] Bhargava, A., Kendrick, D. W., Colket, M. B., Sowa, W. M., Casleton. K. H., Maloney, D. J., 2000, "Pressure Effect on NOx and CO Emissions in Industrial Gas Turbines," Proceedings of ASME Turbo Expo 2000.

Table Captions List

Figure Captions List